Acta Materialia 278 (2024) 120280

Contents lists available at ScienceDirect

Acta Materialia

journal homepage: www.elsevier.com/locate/actamat

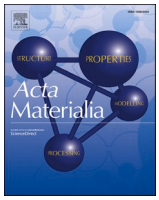

Full length article

3D deep learning for enhanced atom probe tomography analysis of nanoscale microstructures

Jiwei Yu [a], Zhangwei Wang [a,*], Aparna Saksena [b], Shaolou Wei [b], Ye Wei [c], Timoteo Colnaghi [d], Andreas Marek [d], Markus Rampp [d], Min Song [a,*], Baptiste Gault [b,e], Yue Li [b,*]

[a] State Key Laboratory of Powder Metallurgy, Central South University, Changsha, 410083, China
[b] Max-Planck-Institut für Eisenforschung GmbH, Max-Planck-Straße 1, Düsseldorf, 40237, Germany
[c] Ecole Polytechnique Fédérale de Lausanne, School of Engineering, Rte Cantonale, 1015 Lausanne, Switzerland
[d] Max Planck Computing and Data Facility, Gießenbachstraße 2, Garching, 85748, Germany
[e] Department of Materials, Imperial College, South Kensington, London SW7 2AZ, UK

ARTICLE INFO

Keywords:
Atomic-scale characterization
Artificial intelligence
Local chemical ordering
Crystalline defects
Alloy design

ABSTRACT

Quantitative analysis of microstructural features on the nanoscale, including precipitates, local chemical orderings (LCOs) or structural defects (e.g. stacking faults) plays a pivotal role in understanding the mechanical and physical responses of engineering materials. Atom probe tomography (APT), known for its exceptional combination of chemical sensitivity and sub-nanometer resolution, primarily identifies microstructures through compositional segregations. However, this fails when there is no significant segregation, as can be the case for LCOs and stacking faults. Here, we introduce a 3D deep learning approach, AtomNet, designed to process APT point cloud data at the single-atom level for nanoscale microstructure extraction, simultaneously considering compositional and structural information. AtomNet is showcased in segmenting $L1_2$-type nanoprecipitates from the matrix in an AlLiMg alloy, irrespective of crystallographic orientations, which outperforms previous methods. AtomNet also allows for 3D imaging of $L1_0$-type LCOs in an AuCu alloy, a challenging task for conventional analysis due to their small size and subtle compositional differences. Finally, we demonstrate the use of AtomNet for revealing 2D stacking faults in a Co-based superalloy, without any stacking-faults-relevant samples in the training dataset, expanding the capabilities for automated exploration of hidden microstructures in APT data. AtomNet can thus recognize challenging microstructures, including nanoprecipitates with diameters above 2 nm, LCOs with diameters of about 1–2 nm without obvious compositional segregation, and even unforeseen planar defects by analyzing atom-atom environments. AtomNet pushes the boundaries of APT analysis, and holds promise in establishing precise quantitative microstructure-property relationships across a diverse range of metallic materials.

1. Introduction

The overall set of physical properties in materials is governed by microstructures across multiple length scales, spanning from grain-level phase constitution [1–3] down to atomic-level solute distribution [4–6]. Understanding these features necessitates advanced characterization techniques at different length scales for specific applications. Difficulties arise at finer scales, largely owing to the more significant challenges in balancing spatial resolution and statistical reliability [7,8]. Atom probe tomography (APT), with excellent elemental sensitivity and near-atomic resolution [9], can perform a quantitative 3D assessment of nanoscale microstructures in engineering materials and as such allows for direct correlation with macroscopic properties. This includes not only nanoscale precipitates [10–12], complex oxides [13,14] and multiphases [15,16], but also crystalline defects such as dislocations [17,18] and grain boundaries [19,20]. Their successful detection generally depends on a certain degree of compositional segregation. Relevant algorithms include isosurface analysis [21,22], K nearest neighbor [23], radial distribution function [24], maximum separation algorithm [25], core-linkage [23], Gaussian mixture model [26], and hierarchical density-based cluster analysis [27] to visualize or indicate the degree of segregation.

* Corresponding authors.
E-mail addresses: z.wang@csu.edu.cn (Z. Wang), msong@csu.edu.cn (M. Song), yue.li@mpie.de (Y. Li).

https://doi.org/10.1016/j.actamat.2024.120280
Received 18 January 2024; Received in revised form 10 July 2024; Accepted 7 August 2024
Available online 8 August 2024

An obvious limitation occurs when there are subtle or even negligible elemental segregations, as can be the case for local chemical ordering (LCO) [28] or 2D stacking faults [29] that have been reported as challenging to analyze. Deciphering these elusive microstructures in 3D would help establish a concrete structure-property relationship, enabling the manipulation of these structures to design advanced materials. For example, LCO exhibits a different atomic occupation compared to the matrix, which increases the local component fluctuation and thereby decreases the mobility of dislocations [30]. Similarly, LCO can also reduce the width of extended dislocations, explaining why the experimental stacking fault energy is higher than the calculated value [31]. Besides, LCO can affect the atomic spin and orbital magnetic moments, thereby altering the thermal, electrical, and magnetic properties of materials [32,33]. The key to characterizing these elusive microstructural features requires exploiting the partial structural information within APT data.

Following reconstruction, APT data takes the form of a 3D point cloud along with the atomic or ionic identity [34,35]. APT's chemical sensitivity is in the range of 10–100 ppm, but its spatial information is anisotropic due to the trajectory aberrations (the resolution of the best scenario is 0.3 nm in the lateral direction and 0.1 nm in the depth direction) [36,37]. In addition, 20 %–65 % of the ions are randomly lost, because of the limited open area of the particle detector or due to grids with limited transparency on the path of the ions. As a result, the mining of the remaining high-quality yet partial crystallographic information requires expertise, sophisticated tools, and remains both time-consuming and user-dependent [38–41]. Machine-learning-based algorithms are being developed to improve data extraction, simplify and automate data analyses, including user-independent mass spectrometry analysis [42–45], intelligent interface detection [19,46,47], or more complete APT data analysis workflow [48,26].

Another example is the analysis of the partial structural information retrained within APT data [49]. This is typically analyzed through the use of spatial distribution maps (SDMs). The generation of a single SDM requires the integration of signals from a certain volume of atoms (1–2 nm), and the 3D structural data is reduced to 1D- of 2D-histograms enabling the quantification, along specific crystallographic orientations, of inter-atomic distances. Systematically generating and analyzing SDMs large datasets from which millions of SDM patterns require automated analysis workflows as recently enabled by machine-learning [50,51], including for challenging LCO detection [28,52,53].

With APT's point cloud being intrinsically 3D, it is natural to extend these methodologies for extracting microstructural features directly to 3D, going beyond conventional analyses that start with a data dimensionality reduction into 1D/2D descriptors, causing potential information loss [28,37]. Our recent work demonstrated the possibility of applying a 3D convolutional neural network (CNN) to analyze voxelized APT data to segment the 3D distribution of $L1_2$-type nanoprecipitates from a disordered FCC matrix [54]. However, the required data region was limited to specific crystallographic poles and did not address situations where no clear elemental segregations exist. Moreover, the nature of voxelization limited the size range of the recognized domain using CNN, thus not reaching down to the single-atom scale.

Here, we propose a 3D point-cloud-based neural network, named AtomNet, to handle the information at the single-atom level without voxelization to reveal different nanoscale microstructures. AtomNet is based on PointNet [55], which can effectively and robustly handle point cloud data. Prior knowledge about continuous phase distribution is also introduced to AtomNet for better recognition ability. First, AtomNet is tested by 3D imaging nanoprecipitates in an AlLiMg alloy used as a benchmark, and we showcase its ability beyond previous work that would only work in the highest spatial resolution. Then, the more challenging case of the detection of $L1_0$-type LCOs in red gold, which has a composition close to equiatomic AuCu, for which previous segregation-based analysis isosurface failed to identify ordered domains. Finally, the ability of AtomNet to indicate the positions of stacking faults is explored in a Co-based superalloy. The advantages and limitations of AtomNet are discussed, along with directions for future developments.

2. Materials and methods

2.1. Materials

APT data of Al-6.79Li-5.18Mg (at.%, thereafter) alloy annealed at 150 °C for 8 h was selected as a benchmark, as it has been previously used in Ref. [38,54,56]. The data was collected on the Cameca LEAP 3000XSi with a 55 % detection efficiency [56]. A deformed Au-46.8Cu-5.3Ag red gold [57] and Co-based superalloy (Co-32Ni-8Al-5.7W-6Cr-1.8Ta-2.8Ti-0.1Hf-0.4Si) alloy were chosen to show the LCO and defects recognition ability of AtomNet, respectively. The former APT measurement was performed on a LEAP 5000XS with an 80 % detection efficiency, while the latter was on a LEAP 5000XR with a 52 % detection efficiency. All site-specific (along the {002}) needle-like specimens were prepared using the FEI Helios focused ion beam with a Ga ion source. The APT experiments were performed in laser pulsing mode at 50–60 K, 0.8–1.0% detection rate, 40–45 pJ laser energy, and 125–250 kHz pulse rate. APSuite 6.3 was used for all initial reconstructions by tuning two important parameters, i.e. the field factor and image compression factor according to the method introduced in Ref. [58,59].

2.2. Feature engineering

Appropriate feature engineering is a cornerstone of machine learning [60]. APT data has two primary components: the Euclidean spatial coordinates (*X, Y*, and *Z*) of each atom of the point cloud; the other is the mass-to-charge information of each atom to identify the chemical species. Inspired by how scientists distinguish different crystal structures with specific elemental site occupations, a simple and efficient feature extraction method is proposed. For each atom, we extracted its relative 3D atomic position relative to the nearest neighbor (NN), i.e. ΔX ΔY ΔZ, as shown in Fig. 1a. *N* (neighbor) and *S* (self) represent the elemental species of neighboring atoms and the selected atom itself, respectively. Here we use A, B, C … to represent different elements. Compared with voxelization methods, AtomNet exhibits great advantages as shown in Fig. S1, with minimized memory utilization and completely accurate localization. Voxelization will inevitably cause shifts because of the grid approximation. A higher voxelization length can reduce the shifts at the expense of squared (2D) or cubic (3D) memory. By avoiding voxelization, AtomNet can deal with random-shape inputs.

We also studied the relationship between neighbor atom numbers and model performance, as plotted in Fig. S2. As the NN increases, the validation AUC score increases. Because of a combination of limited spatial resolution and limited detection efficiency of APT [61,62], there is a need to define the number of NN (nearest neighbor) beyond the first shell. Even assuming no losses from imperfect efficiency, when the number of NN is low, i.e. 8, even the first shell (12NN in FCC) cannot be entirely captured and AtomNet would inevitably fail to learn the structural information. 32NN-128NN leads to validation AUC scores over 0.90. When the NN reaches 128, the validation AUC score becomes stable, which means distant atoms do not provide additional information for AtomNet to judge structures. In Fig. S3, we visualized the recognition ability of different NNs. It is consistent with the AUC score in Fig. S2, in which a larger NN makes fewer erroneous predictions. A 128NN configuration appears to be an optimal choice. However, the required memory (RAM) would be approximately four times larger compared to using the 32NN, which makes 128NN inefficient and impractical to deploy on our personal computers. Following the feature update strategy, a 32NN configuration can effectively handle noisy atoms, thereby ensuring its reasonability. A lower NN configuration, such as 16NN, is theoretically impractical for LCO analysis since it cannot encompass the entire second shell (18NN in FCC). A higher NN

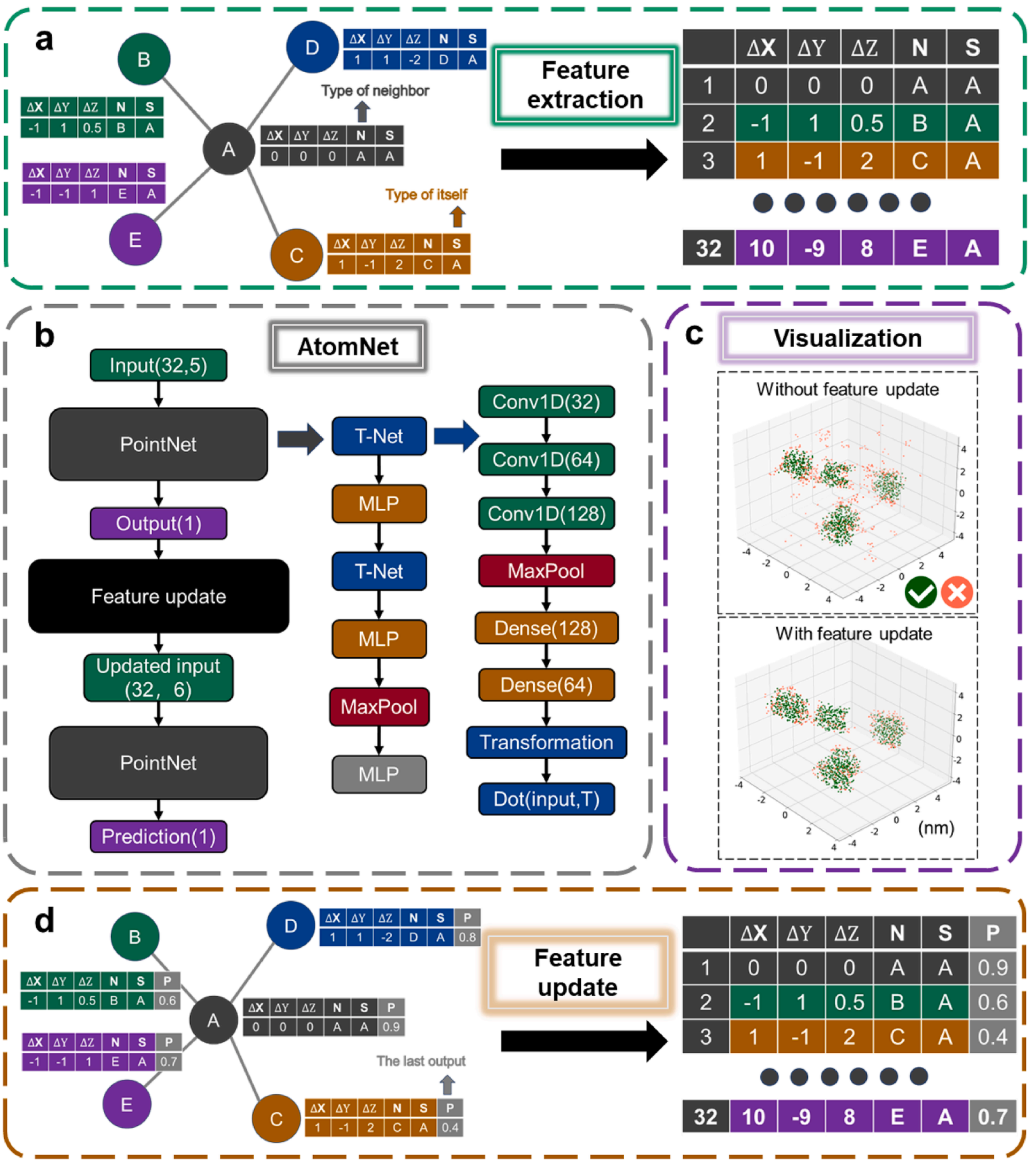

Fig. 1. Overview of the proposed AtomNet architecture. (a) The details of feature engineering of each atom. The left part shows the schematic of sampling information from neighboring atoms in APT data. The right part shows the input feature matrix of the "A" atom. (b) Architecture of AtomNet model. From left to right, AtomNet, PointNet block and T-Net are painted successively. Brackets in AtomNet indicate data shape and in T-Net mean the number of filters/neurons. All activation functions are "Relu" except the output layer which uses "Sigmoid". (c) Visualization of nanoparticles before/after feature updating. Green atoms represent a correct prediction, while red atoms represent an incorrect prediction. (d) Feature updating for incorporating prior knowledge to improve accuracy. (For interpretation of the references to colour in this figure legend, the reader is referred to the web version of this article.)

configuration, such as 64NN, can reduce the number of noisy atoms and achieve a test AUC score of 0.871. However, it still cannot surpass the 32NN with the feature update (test AUC score: 0.901) and requires approximately double the RAM. For other crystal systems, like BCC and HCP, similar tests would need to be performed to determine the best NN.

2.3. *Workflow of AtomNet*

PointNet is a popular 3D neural network that handles point clouds directly and efficiently, respecting the permutation invariance of inputs [55]. This avoids generating large amounts of sparse data and losing information that was encountered when using the CNN-based strategy to transform point clouds into regular 3D voxels, 2D images or 1D curves [37,54]. Here, we propose AtomNet, which utilizes PointNet as a fundamental building block, to identify challenging nanoscale microstructures in APT data. It is worth noting that the name, AtomNet, has been used in the biological field [63], although its structure differs entirely from what is used in this work. As shown in Fig. 1b, the applied PointNet block mainly consists of 2 T-Nets, 3 MLPs and 1 MaxPool layer. The T-Net allows affine transformations such as translation, rotation, shearing, and so on. It was originally designed to ensure 3D spatial invariance. T-Net consists of 3 Conv1D, 2 Dense, 1 MaxPool and 1 Transformation layers, followed by the original input dotting with a transformation matrix to complete the affine transformation. MLP stands for the multi-layer perceptron with 2 to 3 wt shared Conv1D or Dense layers. MLP is the primary computational processing unit, and traditional artificial neural networks could be constructed only with it. MaxPool is a pooling or aggregating layer that stores the maximum value and discards others, providing interactions within nearby atoms. After training the first PointNet block, AtomNet shows moderate predictive ability, for example, with the obtained AUC (area under the receiver operating characteristic curve) value being 0.78 in the Au-Cu alloy.

To further improve model performance, a feature updating strategy

was utilized to introduce prior knowledge, as an inductive bias [64] to help model learn specific notions efficiently. Here, the notion refers that precipitates, LCOs or distinct phases usually consist of continuous and compact groups of atoms. If most of the neighbor atoms belong to the specific phase, the target atom would also belong to the same phase. The original features were updated after the first PointNet block, as shown in Fig. 1b. Then the updated features were fed into the second PointNet block, and a higher AUC of 0.86 was obtained in the Au-Cu alloy. Fig. 1c visualizes the results before and after the first feature update, suggesting that the number of incorrectly predicted atoms has been greatly reduced. Fig. 1d shows the detail of feature update, by adding/updating predictions from the last PointNet block. Theoretically, this iteration can be repeated to get better performance, at the expense of heavy computations. A detailed test is provided in Section 2.5.

2.4. Simulated data bank

As a supervised algorithm, AtomNet requires reliable training datasets. Here, a pipeline is proposed to generate synthetic APT point cloud datasets by simulating the trajectory aberration and imperfect detection efficiency encountered in APT experiments [58]. As shown in Fig. 2, the simulation can be concluded as 4 steps: create perfect structures, add specific domains, rotate, and add noise. In step 1, a perfect 3D FCC-matrix superlattice was built with a size of $4 \times 4 \times 4$ nm^3. The structure originated from a single cell and expanded into a cube, maintaining periodicity. First, 1 vertex atom ({0, 0, 0}) and 3 face center atoms ({0.5, 0.5, 0}, {0.5, 0, 0.5}, {0, 0.5, 0.5}) were identified. Subsequently, these 4 atoms were expanded into the FCC structure using 'for' loops. In step 2, different kinds of domains were inserted. Spherical $L1_2$ ($Al_{0.75}Li_{0.2}Mg_{0.05}$), $L1_0$ (AuCu), and $L1_2$ ($Co_{0.4}Ni_{0.35}Al_{0.095}W_{0.043}X$, X representing all remaining elements) nano-domains were embedded into an FCC matrix of Al-Li-Mg, Au-Cu and Co-based superalloys, respectively. Stress-related lattice distortions from a lack of coherency are neglected, since our simulations are performed on a rigid lattice, and offsets within APT data arising from trajectory aberrations are usually much more significant than the distortion from a lack of coherency. The lattice distortion induced by stress should be considered when investigating precipitates with incoherent interfaces with the matrix, particularly focusing on distortions along the depth direction with a high resolution. In step 3, the superlattice was rotated to simulate experimental data along different crystallographic orientations, allowing to simulate regions of high and low spatial resolution (i.e. near and away from crystallographic poles). As listed in Table 1, AlLiMg alloy was randomly rotated to $\pm 90^\circ$ to simulate all possibilities of crystallographic orientations. While for the other two systems, the rotation along the x

Table 1
Parameters of simulated data in different alloying systems.

Alloys	$L1_2/L1_0$-domain radius (nm)	Rotation (°)		Detection efficiency	Trajectory aberration (nm)	
		X/Y	Z		X/Y	Z
Al-Li-Mg	1.2–2.0	±90	±90	40 %–80 %	0.2–0.5	0.08–0.02
Au-Cu	0.8–1.2	±3	±90	40 %–80 %	0.2–0.5	0.08–0.02
Superalloy	1.4–2.0	±3	±90	40 %–80 %	0.2–0.5	0.08–0.02

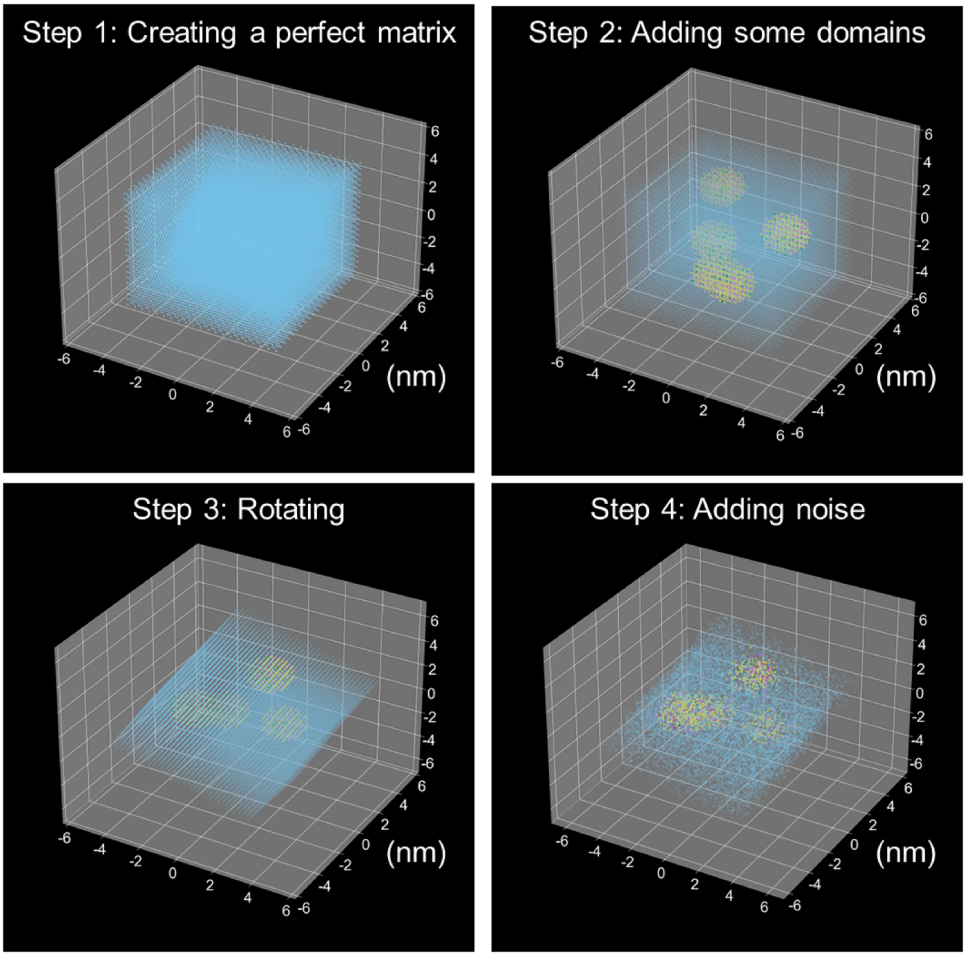

Fig. 2. Pipeline of simulated APT data. Adding some specific nano-structures ($Al_{0.75}Li_{0.2}Mg_{0.05}$ nanoparticles here) into a perfect FCC matrix, then rotating and disturbing to simulate the crystallographic orientation and trajectory aberration encountered in APT data, respectively.

and y axis was limited to ±3° and along the z axis was randomly chosen between ±90° to simulate experimental data along the {002} pole. Note that the local rotations along x and y are intended to reflect the local distortion of the atomic planes along the pole [61]. Rotation, being a linear transformation, is efficiently achieved by applying a rotation matrix. In step 4, atoms were disturbed and discarded to simulate the noise. Gaussian noise was added to shift atoms in 3D to simulate trajectory aberration, with a Gaussian distribution having a standard deviation of 0.2–0.5 nm in the x/y directions and 0.08–0.2 nm in the z direction. Certain fractions of atoms were removed to simulate the detection efficiency, with a random value between 20 % and 60 %. All steps are compiled into Python codes, available at https://github.com/bookofstrange/AtomNet.

2.5. Training details

AtomNet was implemented by the TensorFlow-GPU 2.10.0 backend on Python 3.9.7. Training/validation/testing data contained 80/10/10 cubes with a 4/4/10 nm length, respectively. Training and validation data are limited to under 4 nm, to increase the simulation diversity and decrease the computational cost. The cube length of 4 nm is decided by the maximum domain size set to 4 nm. The training/validation ratio is set by the standard protocol, which is 8/1. Each 4-nm cube included 1500–3800 atoms, depending on the detection efficiency. After a thorough tuning procedure, the chosen loss function was BinaryCrossEntropy and the optimizer was Adam (adaptive moment estimation) with a learning rate of 10^{-3}. BinaryCrossEntropy (H) can be calculated as below:

$$H = -\frac{1}{N}\sum_{i=1}^{N} y_i \cdot \ln(p(y_i)) + (1-y_i)\cdot \ln(1-p(y_i)) \quad (1)$$

Where N is the total sample number, y_i is the ith label, and $p(y_i)$ is the ith predicted probability of being true. AUC was used as the metric to measure unbalanced datasets (the ratio of atoms between the labeled $L1_2$/$L1_0$-domain and the matrix is close to 1:4). Loss/BinaryCrossEntropy is a differentiable function that helps gradient descent during training. Metric/AUC is the decisive factor of model performance. For the training procedure, the chosen batch size was 256, and callbacks were used to monitor and save the best model. An Au-Cu example of the evolution of AUC and loss is shown in Fig. 3. The change in background color indicates the feature updating by training another PointNet block. The obtained AUC value in the validation dataset increases significantly from about 0.78 to 0.86 after the first update due to the introduced prior knowledge, while the loss increases from about 9.22 to 9.45 at the same time. The higher loss may be related to the newly added dimension, which introduces more variables and uncertainties. Thus, we pay more attention to AUC instead of loss when evaluating the obtained classification model [65]. Based on the balance between the AUC value and computation costs, the number of PointNet blocks in the Al-Li-Mg, Au-Cu, and Co-based superalloy is 2, 3, and 2, respectively.

3. Application of AtomNet

3.1. Nanoprecipitates in AlLiMg

Nanoscale precipitates play a critical role in influencing the mechanical properties of alloys primarily through precipitation hardening mechanism [1,2,12,66]. Quantifying these nanoprecipitates is beneficial for establishing microstructure-property relationships that can help further in designing advanced materials [67,68]. The Al-Li-Mg dataset used in Ref. [38,56] was used as a benchmark to test AtomNet. Fig. 4a shows an example of the simulated $L1_2$-type Al_3(Li, Mg) particles with a radius of 1.2–2 nm embedded in a disordered FCC matrix. AtomNet accurately predicted if an atom belongs to the $L1_2$ phase, as shown in Fig. 4b. Isosurface can also capture these nanoprecipitates but some of them are shrunk in size, as shown in Fig. 4c. After performing once feature updating strategy mentioned in Section 2.3, the final AUC score is 0.890±0.033. The AUC reflects how well the model is trained on unbalanced datasets (See Section 2.5), but not sufficient to judge the recognition ability for each class.

Recall and precision metrics were used to further assess the recognition ability, as displayed in Fig. 4c and d. Recall is a metric that reflects how many positive samples can be detected, while precision tracks the reliability of predictions, defined as below:

$$\text{Recall} = \frac{\text{Total number of correctly predicted oredered atoms}}{\text{Total number of truely oredered atoms}} \quad (2)$$

$$\text{Precision} = \frac{\text{Total number of correctly predicted oredered atoms}}{\text{Total number of predicted oredered atoms}} \quad (3)$$

AtomNet obtained an overall recall and precision of 0.79 and 0.72 (Fig. 4), while isosurface had an overall recall and precision of 0.51 and 0.73. The metric difference is consistent with the visualization: the lower recall of the isosurface method leads to fewer atoms being recognized, resulting in an apparent size shrinkage. It is interesting to note that both recall and precision of Li are higher than those of Al and Mg elements, which can be explained by its higher tendency for

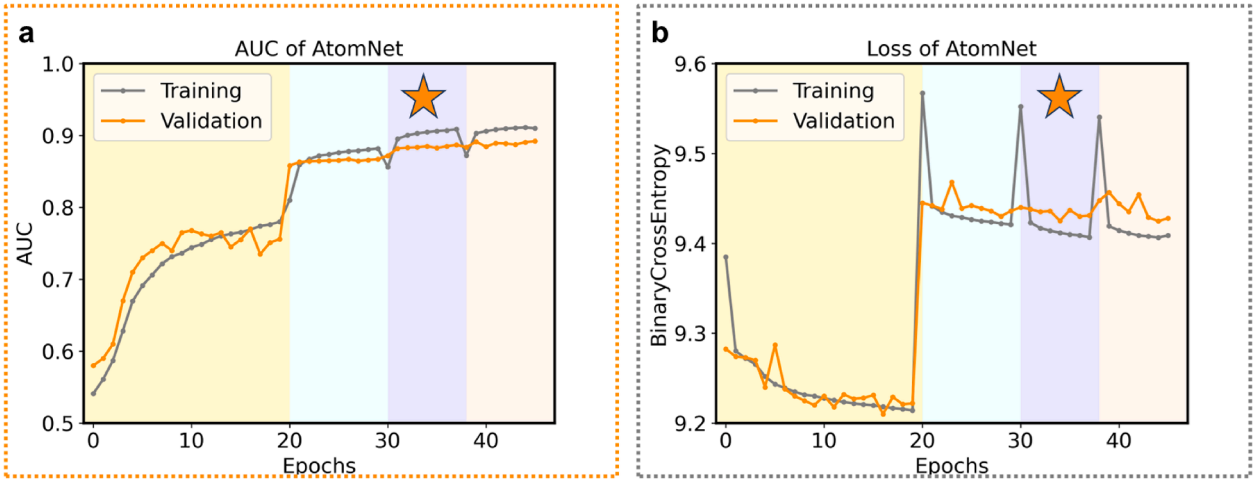

Fig. 3. Training and validation of AtomNet. (a) AUC and (b) loss of AtomNet with epochs in the Au-Cu system. The background color will change after adding another PointNet block with the updated features. The orange star marks the final choice. (For interpretation of the references to colour in this figure legend, the reader is referred to the web version of this article.)

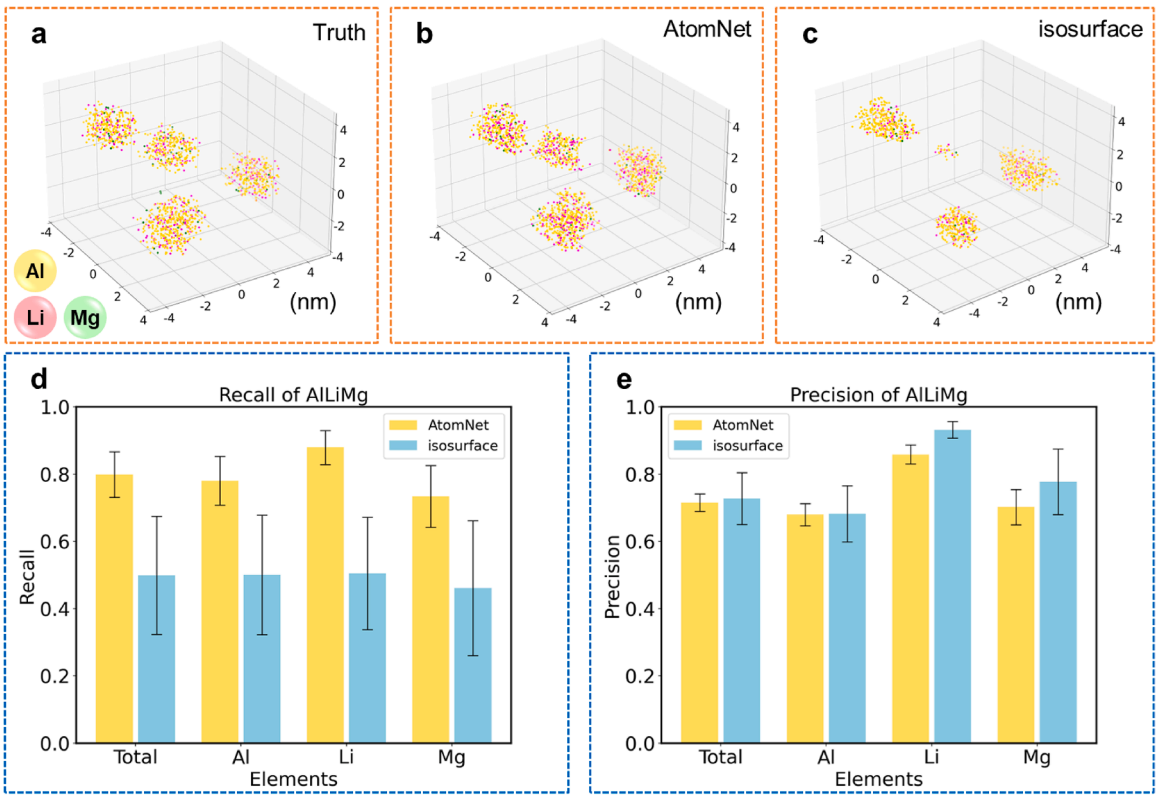

Fig. 4. Performance of AtomNet on the simulated AlLiMg test datasets. (a) An example of some simulated $L1_2$ nanoprecipitates. (b) and (c) are the corresponding predicted results of AtomNet and the 8 at.% Li isosurface, respectively. Only atoms from nanoprecipitates are shown. (d) Recall and (e) precision from different elemental species, respectively. 10 cubes with a length of 10 nm were analyzed to obtain a statistical result with the default classification threshold of 0.5 (a more detailed discussion about the choice of thresholds will be given later).

partitioning between the ordered precipitates (20 at.%) and the disordered matrix (5 at.%). This first example showcases AtomNet's capability for reliably identifying $L1_2$-ordered precipitates in simulated datasets, and some initial advantages compared to isosurface.

AtomNet was then applied to the experimental data, both close to and away from the {110} pole, in regions-of-interest indicated in the detector hit map shown in Fig. 5a. Analysis of structural information in APT can normally be done only in regions near poles, i.e. where the corresponding crystallographic planes are imaged. Fig. 5b shows nanoprecipitates captured by AtomNet, at the {110} pole. Fig. 5c shows the distribution of $L1_2$ particles marked by an 8 at.% Li isosurface. The AtomNet prediction closely matches the isosurface result, with similar average size and spatial locations.

AtomNet is also consistent with the previous CNN method (Fig. 5d) [38]. It's a voxelization method and can only work along specific pole sites. The prediction is based on cubes of a certain size, so the interface between the matrix and the nanoparticles is facetted. Instead, AtomNet sets out from every single atom and thus can retain the intrinsic nature (nearly atomic resolution) of APT data. Moreover, the blue box in Fig. 5d marks one missing nanoprecipitate via CNN, although it ought to exist (compared with Fig. 5b and Fig. 5c). Third, as compared to previous CNN result, some noisy points/atoms remain via AtomNet due to its single-atom nature, which may be eliminated with a clustering algorithm by setting the minimum number of atoms in a cluster.

We further obtained the spatial distribution maps along the depth direction (z-SDMs) [69] of Al-Al pairs of the recognized $L1_2$ particles and remaining matrix, as shown in Fig. 5e. The matrix has an interplanar distance of 0.14 nm while the $L1_2$ nanoparticle has an interplanar distance of 0.28 nm. This difference relates to the atomic occupancy of Al, which is random in FCC and face-centered in $L1_2$, as discussed in Ref. [56].

Poles are not always visible or planes imaged, and this has limited the application of previous approaches to small reconstructed volumes near poles. As Fig. 5f and g reveal, AtomNet can also detect precipitates in the subset of the data in which atomic planes are not imaged, and these agree well with segmentation based on isosurface. Although AtomNet was trained using spherical particles, this example demonstrates that non-spherical domains (Fig. 5f) can be identified.

3.2. *Local chemical orderings in red gold*

The last case study exhibits obvious elemental segregations, which can also be handled using other approaches. Here, we will further explore the performance of AtomNet in a more challenging case with LCOs. Red gold is generally considered to have a transformation from FCC to the ordered $L1_0$ phase, which hardens the material but limits its workability [57]. An interesting shape memory effect is also related to this $L1_0$ phase [70]. In-situ synchrotron X-ray diffraction technique indicated the presence of LCOs by observing weak peaks [57] or peak dissymmetry [71], however the characterization of the early stage of $L1_0$ ordering remains challenging due to the lack of obvious segregation, coherent interfaces with the matrix, and the small size of the ordered domains (typically below 2 nm). Here we apply AtomNet to capture these tiny $L1_0$-type LCOs. Note that the isosurface approach cannot work here due to the absence of obvious compositional differences between LCOs and FCC matrix.

First, AtomNet was tested on simulated datasets. As displayed in Fig. 6a, we built several $L1_0$ LCO domains with a diameter of 1.6 nm embedded in FCC matrix. After simulating the 40 % detection efficiency, a domain would only contain in the range of 50 atoms, making its detection arduous compared to larger precipitates as in Al-Li-Mg. This analysis achieved an AUC score of 0.822±0.052 on test datasets when using the default threshold of 0.5, while the predicted LCOs experienced significant size shrinkage in Fig. 6b (the average radius is reduced from

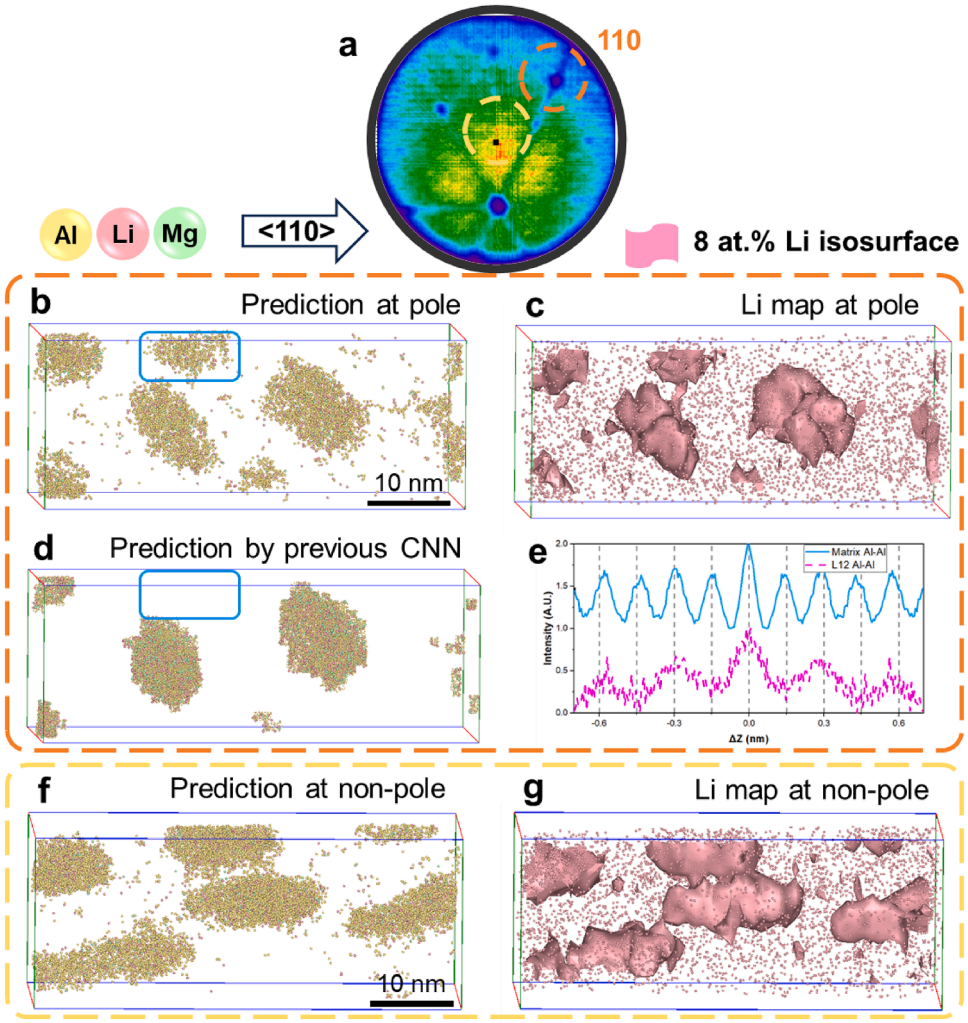

Fig. 5. Validations on AlLiMg experimental data. (a) 2D detector hit map to highlight the pole and non-pole sites for further analysis. The orange circle marks {110} pole, while the yellow circle is non-pole. Reconstructions are based on pole (b, c, d) and non-pole (f, g) respectively. (b) is the prediction by AtomNet. Here only nanoprecipitates are displayed. (c) is the isosurface method to show nanoparticles on Li maps. The concentration threshold is 8 at.% Li. (d) Prediction with previous CNN method [30]. Blue box in (d) marks a missing nanoprecipitate. (e) z-SDMs of Al-Al pair of nanoprecipitates and the remaining matrix from (d). (f) and (g) are predictions by AtomNet and isosurface respectively, at non-pole sites. (For interpretation of the references to colour in this figure legend, the reader is referred to the web version of this article.)

about 0.8 nm to about 0.6 nm). To improve the shape and size accuracy of predicted LCOs, different thresholds were compared. At a lower threshold of 0.3, Fig. 6c, the size of the detected LCOs looks closer to the ground truth compared to those obtained with a threshold of 0.5, although it appears to get more noise. A higher threshold of 0.7, Fig. 6d, only leaves a few atoms per domain due to the strict classification criterion. We also assessed the relationship between threshold and recall/precision, which showed a trade-off in Fig. 6e and Fig. 6f. As the threshold increases, the precision tends to increase while the recall tends to decrease. Recall shows how many of positive samples (LCOs here) can be found. Precision shows the probability of being true (LCOs here) from all recognized samples. Detecting out (recall) is the precondition of recognizing right (precision). Since LCOs are not easy to detect, guaranteeing a higher recall is the better choice. When the threshold is 0.3/0.5/0.7, accordingly, the recall and precision are (0.72 0.52)/(0.53 0.69)/(0.28 0.87). A threshold of 0.3 leads to recall exceeding 0.7 and maintains precision at 0.5. That means 72 % of true LCO atoms will be successfully detected and only 48 % of the detected samples are fake. By adding recall and precision when the threshold is 0.2/0.3/0.4/0.5/0.7, one obtains 1.20/1.24/1.23/1.22/1.15, which again points to a threshold of 0.3 being the optimal value. Henceforth, the threshold of 0.3 is finally decided for this case.

Fig. 7a shows the obtained distributions of 3D $L1_0$ LCO domains along the {100} pole, and in Fig. 7b each identified domain is displayed with a separate color. Note that the clustering method in APSuite 6.3 was applied to assess the size distribution of LCO domains with a maximum separation distance of 0.4 nm and a minimum number of ions in the cluster of 3. The domain appears spherical. Fig. 7c plots the z-SDMs of different elemental pairs in the matrix (FCC) and LCO domains. Both peak-to-peak distances of Au-Au and Cu-Cu z-SDMs are half than those in LCOs, which is consistent with the expected crystal structures (FCC and $L1_0$). The distribution of size (number of atoms) versus count of LCOs is given in Fig. 7d, and compared with that from a chemically randomized dataset. The latter was generated by maintaining the x, y, and z coordinates but randomly shuffling the mass-to-charge and the associated elemental identities [28,52]. We compare the size distributions of four randomized datasets with each other based on the contingency coefficient (μ) [52]. The upper limit of the obtained μ being near 0.25 is regarded as a baseline for these randomized size distributions in experimental data. After analyzing the experimental data, an average value of 0.270±0.011 was obtained, which suggests the occurrence of non-statistical $L1_0$-LCOs in this system. A fraction of LCO domains with

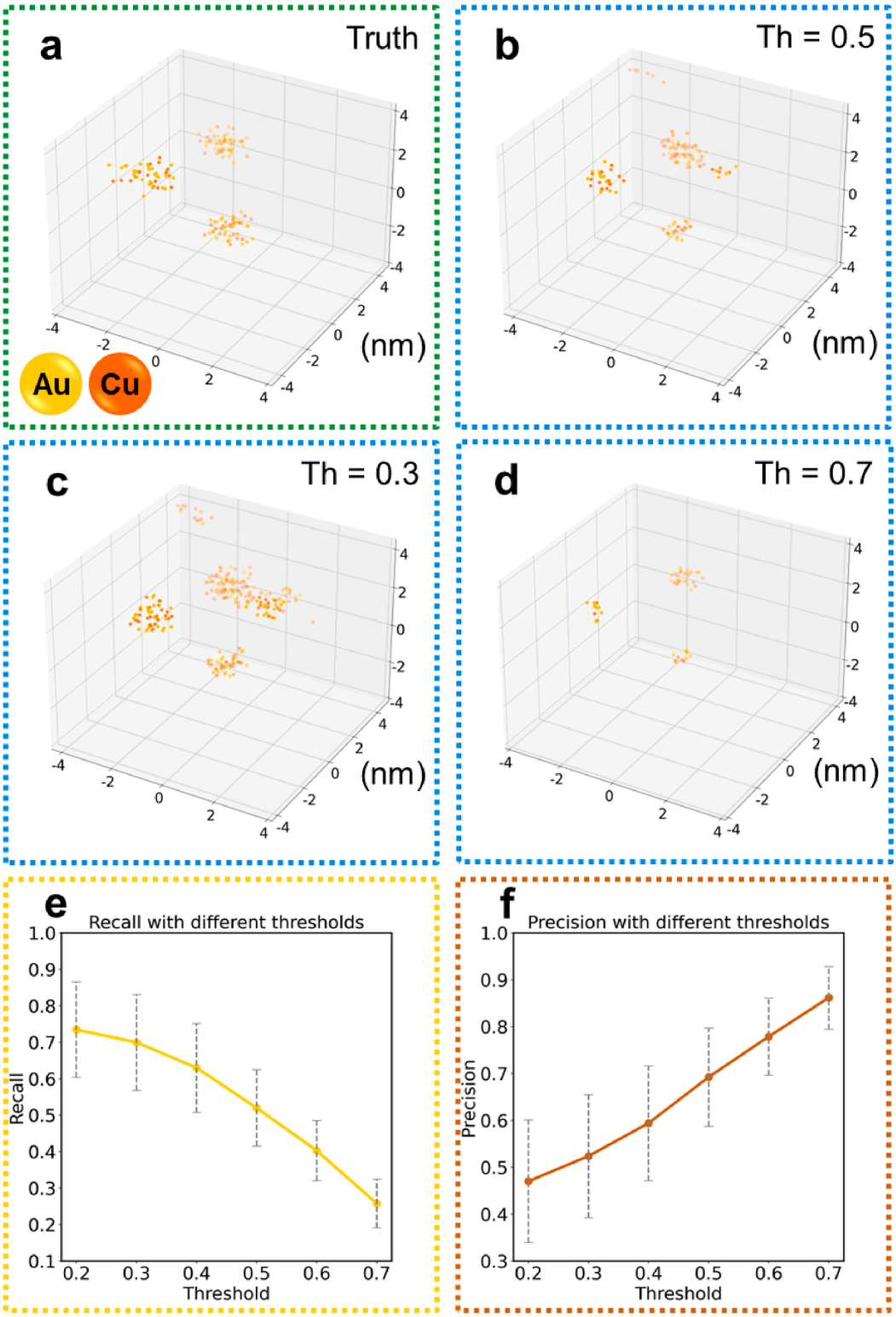

Fig. 6. Trade-off between recall and precision in simulated Au-Cu test dataset with $L1_0$ LCOs. (a) Ground truth of simulated $L1_0$ LCOs with a diameter of 1.6 nm. The matrix is hidden. (b), (c), and (d) are corresponding predictions by AtomNet with different thresholds (represented by "Th" with the value from 0 to 1). (e) and (f) The evolutions of recall and precision with varied thresholds, respectively. 10 cubes with a length of 10 nm were analyzed to obtain the statistical result.<AuQuery: Please check,Part designations in figure legends should be in normal typeface (not bold face).>

>65 APT-counted atoms (> 1.1 nm in diameter) exist in the experimental data while no significant sign in the randomized dataset. This suggests that these small LCO domains with sizes below 65 atoms are primarily formed statistically and randomly in this studied alloy.

3.3. Stacking faults in a deformed co-based superalloy

Stacking faults (SFs) are 2D crystallographic defects along which the stacking of {111} close-packed planes is out of order [72,73]. SFs reduce the dislocation mobility in single crystal superalloys, and affect their

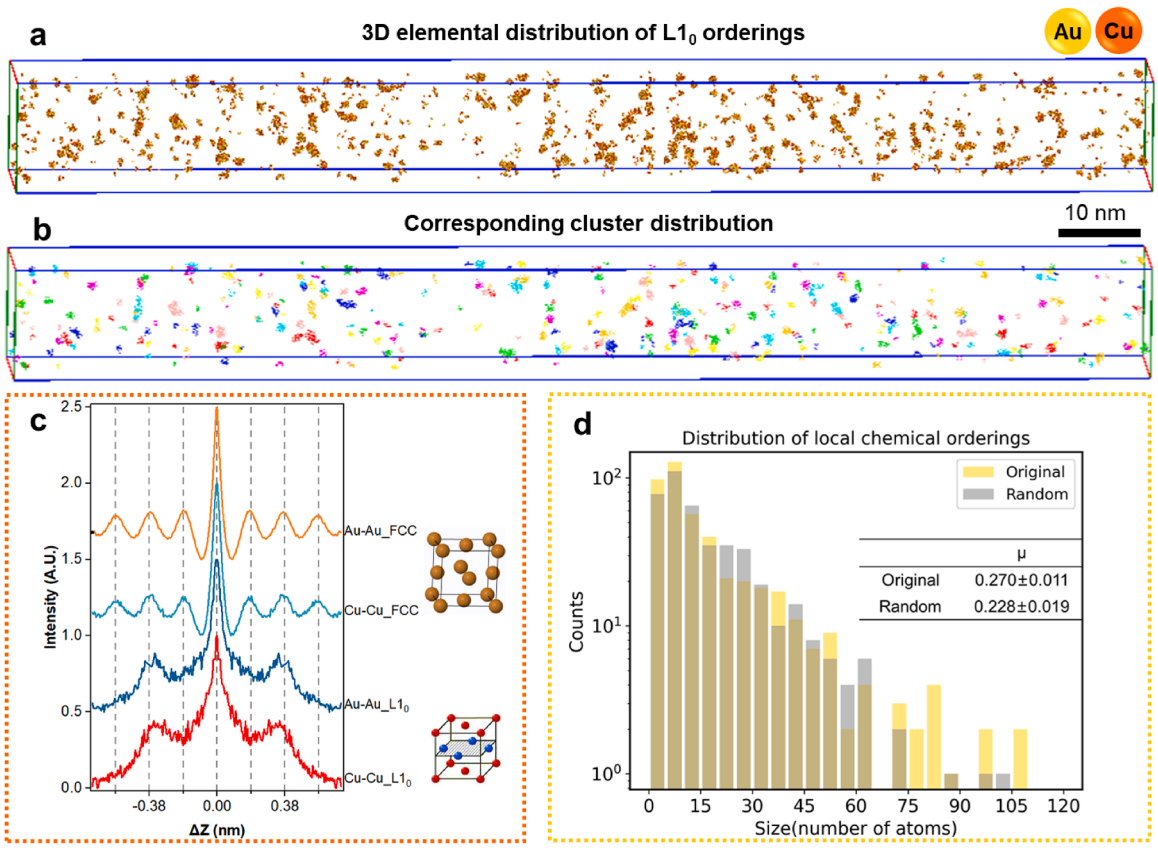

Fig. 7. 3D distribution of $L1_0$-typed LCOs in Au-Cu along the {100} pole. (a) Elemental distributions predicted by AtomNet. (b) Corresponding cluster distribution in (a). (c) Au-Au and Cu-Cu z-SDMs from $L1_0$-typed LCOs in (a) and remaining FCC matrix. The right part displays the ideal crystal structure of matrix (FCC) and LCOs ($L1_0$). (d) Size distribution of $L1_0$-typed LCOs in (b). A chemical-randomized dataset is compared. The inserted table gives a μ value, a parameter that indicates the degree of randomization.<AuQuery: Please check,Part designations in figure legends should be in normal typeface (not bold face).>

creep responses [74,75]. Recent studies also suggested that deformation faults could be used to further design metastable alloys [8,72,76], as they can serve as the loci for local phase formation and transformation [77–79]. This motivates the third application of AtomNet. Assessing the potential presence of SFs within APT data is however challenging, and has often required the use of correlative electron microscopy [29], and depends on the degree of elemental segregations to the SFs, which is unknown beforehand and can be subtle. Here, we considered a deformed Co-based superalloy as an example to explore the potential of AtomNet on recognizing unforeseen patterns associated with defects like SFs. Since SFs are usually associated with dislocations and potential segregations, simulating realistic SFs remains challenging. Besides, phase structure or atomic occupation has infinite permutations in material science. Using AtomNet to search for SFs without simulating SFs explicitly was a way to test AtomNet's behavior in such a context. The training data only consists of the $L1_2$ phase ($Co_{0.4}Ni_{0.35}Al_{0.095}W_{0.043}X$) and FCC matrix. In case AtomNet converged quickly by elemental information, we adjusted the component of matrix and precipitate to be the same, forcing AtomNet to focus on structural information and giving a sign when the atomic occupation is different ($L1_2$ here). Fig. 8a shows data containing primarily a $L1_2$-ordered γ' precipitate, with only a small volume of the FCC γ–matrix. Based on previous reports [29,80,81], SFs have so far been sought by depletion in the Al concentration projection map, as shown in Fig. 8a, in which subtle planar variations are observable.

Here, two zones marked in Fig. 8a were analyzed using AtomNet to automatically search the sites of SFs. In Zone 1 (Fig. 8b), a reduction in the density map of ordered domains is marked by the red arrow, indicating a zone in which the atomic organization is not the $L1_2$ phase and thus possibly a SF. Zone 2 (Fig. 8c) exhibits a vertical wide zone with a low density of $L1_2$-ordered domains, marked by the gray arrow, which was found to go through the entire volume and corresponds to a crystallographic pole. Another zone with a lower density marked by the green arrow can be associated with a SF. AtomNet can hence indicate the position of defects, even without relevant training data.

4. Discussion

In this work, a point-cloud-based AtomNet was proposed to intelligently dig out microstructural information hidden within APT data. We successfully applied it in a series of FCC-based case studies with nanostructures spanning from 3D to 2D. AtomNet offers several advantages over previous methods based on isosurface thresholding [34,35] or CNN-assisted APT analyses [38,54]. First, unlike previous CNN methods based on voxelization, AtomNet handles every single atom. For instance, the segmentation from AtomNet exhibits a smooth phase boundary while previous methods show an obvious jagged boundary (Fig. 5c, d). Moreover, previous methods partially focus on either the compositional differences, i.e. isosurface, or the structural changes, CNN-APT [38]. AtomNet considers both compositional and structural information simultaneously, by integrating features from 32 nearest neighbors with respect to each atom. These features were transformed and trained via a PointNet block to tackle some challenging situations – including, for instance, precipitates imaged away from regions in which atomic planes are imaged in the case of the AlLiMg alloy (Fig. 5), small LCO domains without obvious compositional segregation in Au-Cu (Fig. 7). Third, AtomNet can indicate nanostructures that do not exist in the training datasets, like SFs in the Co-based superalloy. In this case, the composition of the matrix and precipitates was the same in the simulated data, to focus AtomNet only on the structural information. Thus, AtomNet will

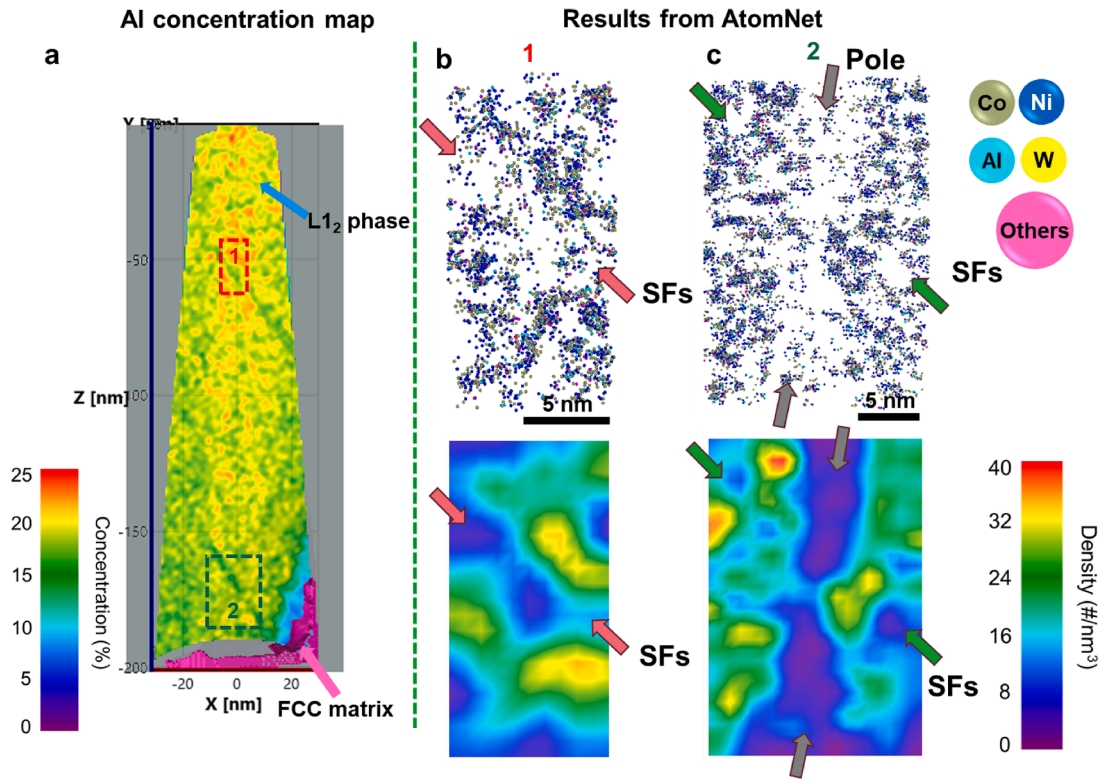

Fig. 8. Exploration in a deformed Co-based superalloy ($Co_{0.4}Ni_{0.35}Al_{0.095}W_{0.043}X$, X represents remaining elements) with SFs. (a) Traditional 2D Al concentration projection map to indicate potential sites of SFs. Two zones inside the $L1_2$ phase were analyzed by the proposed AtomNet. Predictions of AtomNet in (b) zone 1 and (c) zone 2 with atom (up) and density (bottom) maps. Arrows indicate the sites of SFs and the pole. The classification threshold is 0.5.

respond to those never-seen defects by judging the occupations of atoms. Better performance could be achieved if these defects could be simulated and then used to train AtomNet. Last but not least, AtomNet still works well in non-spherical nanodomains whose composition differs from the simulated one like Figs. 5 and 7, further demonstrating its robustness.

Nevertheless, AtomNet has some limitations. For a specific alloy, relevant training data need to be acquired from either experiments or simulations. While conventional methods like isosurface only require manual analysis and trial and error. Of course, this cannot work in the case of Au-Cu with the existence of LCOs.

For the Au-Cu case, the classification threshold was adjusted to test the performance of the recognition model. A trade-off between the recall and precision (corresponding to the size and count accuracy, respectively) is inevitable (Fig. 6e and f). When choosing a low threshold (Fig. 6c), AtomNet achieves a high recall, i.e., a high size accuracy, which is desired for size-focused research. However, the corresponding precision is low and AtomNet falsely classifies more random atoms as ordered ones, i.e., over-recognition phenomenon. By selecting a high threshold (Fig. 6d), AtomNet will get a high precision, i.e., a high count accuracy, which is better for number-density-focused research. For some tasks like detecting $L1_2$ from FCC in the AlLiMg with obvious segregation and relatively large size (above 2-nm diameter), selecting the default threshold of 0.5 would be appropriate for the most time (Figs. 4 and 5). For some challenging tasks like recognizing $L1_0$ LCOs in the Au-Cu with weak segregation degree and small size (below 2-nm diameter), a lower threshold, like 0.3, can ensure that atoms belonging to the hidden nanostructures are recognized as complete as possible. To further validate the reasonability of the selected threshold of 0.3, we analyzed the z-SDMs of the atoms with a threshold between 0.3 and 0.5. The double interplanar spacing still existed for this part of data like Fig. 7c, suggesting its nature of $L1_0$-typed structure.

Our previous work [28,52] has the ability to detect LCOs, even smaller chemical short-range orders (approx. 0.5 nm in radius), focusing more on structural information. However, as highlighted in the introduction, this necessitates the transformation of 3D point cloud data into 1D signals, a computationally intensive process that is circumvented in the proposed AtomNet. While AtomNet facilitates the detection of LCOs in the Au-Cu alloy, its optimal performance lies in characterizing chemical medium-range orders, approximately 0.6 nm in radius. AtomNet exhibits less satisfactory performance in recognizing smaller chemical short-range orders, attributed to the disturbance caused by lateral atoms with lower resolution.

The current approach deals with FCC-based alloys, but it can be easily extended to other structures (BCC, HCP) without limiting the number of components. This would broaden the capability and application of AtomNet, including e.g. compositionally-complex alloys or recognizing grain boundaries in nanocrystalline materials. Moreover, better performance of AtomNet could be achieved with more realistic training datasets, which can be synthesized via advanced generation models like generative adversarial networks [82] and diffusion models [83]. Finally, the recognized accuracy of AtomNet is dependent on the data quality, like the detection efficiency and spatial resolutions. With the improvement of data quality, the boundary of AtomNet can be pushed to more complex situations, even for the detection of 1D (like dislocations) and 0D (like vacancies) nanoscale features.

5. Conclusions

In this work, we designed a 3D deep neural network named AtomNet to intelligently mine hidden nanoscale 3D/2D features from APT data in various FCC-based metallic materials. During training, a crucial feature updating strategy was introduced to achieve a better recognition ability. AtomNet considers both the compositional and structural information, and enables to recognize different microstructures at the singe-atom level, ranging from nanoprecipitates in the AlLiMg, LCOs in the Au-Cu, and even 2D SFs in the Co-based superalloy. AtomNet outperforms

previous isosurfaces and CNN-APT methods in its ability to detect nanoprecipitates independently of the presence of crystallographic orientations and to reveal small LCOs without obvious elemental segregation. AtomNet has the ability to display unforeseen structures that are not present in the training data, such as SFs in the Co-based superalloy. In the near future, AtomNet will be extended to include other crystal structures (BCC, HCP) and more complex compositions, and enable the detection of grain boundary and dislocation.

Data availability

The key data that support the findings are involved in this paper. Other data are available from the corresponding authors upon reasonable request. The AtomNet code is available at https://github.com/bookofstrange/AtomNet.

CRediT authorship contribution statement

Jiwei Yu: Writing – review & editing, Writing – original draft, Visualization, Methodology, Investigation, Formal analysis. **Zhangwei Wang:** Writing – review & editing, Supervision, Funding acquisition, Conceptualization. **Aparna Saksena:** Writing – review & editing, Investigation. **Shaolou Wei:** Writing – review & editing. **Ye Wei:** Writing – review & editing. **Timoteo Colnaghi:** Writing – review & editing. **Andreas Marek:** Writing – review & editing. **Markus Rampp:** Writing – review & editing. **Min Song:** Writing – review & editing, Supervision, Conceptualization. **Baptiste Gault:** Writing – review & editing, Supervision, Conceptualization. **Yue Li:** Writing – review & editing, Writing – original draft, Visualization, Supervision, Methodology, Investigation, Funding acquisition, Formal analysis, Conceptualization.

Declaration of competing interest

The authors declare that they have no known competing financial interests or personal relationships that could have appeared to influence the work reported in this paper.

Acknowledgments

Yue Li acknowledges the research fellowship provided by the Alexander von Humboldt Foundation. We also acknowledge funding from the Max Planck research network on big-data-driven materials science (BiGmax) and the Open Foundation of State Key Laboratory of Powder Metallurgy at Central South University, Changsha, China. Min Song acknowledges the financial support from the Science and Technology Innovation Program of Hunan Province (No. 2022RC3035). A.S. acknowledges the financial support from Deutsche Forschungsgemeinschaft (DFG) under project A4 of the collaborative research center SFB/TR 103. The Co-based superalloys were provided by A. Bezold and S. Neumeier as part of the collaborative work pursued in the same SFB/TR 103, Project B3. Paraskevas Kontis is acknowledged for providing the Au-Cu APT data. Stefan Bauer is acknowledged for fruitful discussion.

Supplementary materials

Supplementary material associated with this article can be found, in the online version, at doi:10.1016/j.actamat.2024.120280.

References

[1] Z.W. Wang, W.J. Lu, H. Zhao, C.H. Liebscher, J.Y. He, D. Ponge, D. Raabe, Z.M. Li, Ultrastrong lightweight compositionally complex steels via dual-nanoprecipitation, Sci. Adv. 6 (46) (2020).
[2] S.H. Jiang, H. Wang, Y. Wu, X.J. Liu, H.H. Chen, M.J. Yao, B. Gault, D. Ponge, D. Raabe, A. Hirata, M.W. Chen, Y.D. Wang, Z.P. Lu, Ultrastrong steel via minimal lattice misfit and high-density nanoprecipitation, Nature 544 (7651) (2017) 460–464.
[3] Z.M. Li, K.G. Pradeep, Y. Deng, D. Raabe, C.C. Tasan, Metastable high-entropy dual-phase alloys overcome the strength-ductility trade-off, Nature 534 (7606) (2016) 227–230.
[4] N. Ren, J. Li, R.Y. Zhang, C. Panwisawas, M.X. Xia, H.B. Dong, J.G. Li, Solute trapping and non-equilibrium microstructure during rapid solidification of additive manufacturing, Nat. Commun. 14 (1) (2023).
[5] T. Yang, Y.L. Zhao, W.P. Li, C.Y. Yu, J.H. Luan, D.Y. Lin, L. Fan, Z.B. Jiao, W.H. Liu, X.J. Liu, J.J. Kai, J.C. Huang, C.T. Liu, Ultrahigh-strength and ductile superlattice alloys with nanoscale disordered interfaces, Science 369 (6502) (2020) 427–432.
[6] L. Xie, L. Yin, Y. Yu, G. Peng, S. Song, P. Ying, S. Cai, Y. Sun, W. Shi, H. Wu, N. Qu, F. Guo, W. Cai, H. Wu, Q. Zhang, K. Nielsch, Z. Ren, Z. Liu, J. Sui, Screening strategy for developing thermoelectric interface materials, Science 382 (6673) (2023) 921–928.
[7] A. Shibata, I. Gutierrez-Urrutia, A. Nakamura, G. Miyamoto, Y. Madi, J. Besson, T. Hara, K. Tsuzaki, Multi-scale three-dimensional analysis on local arrestability of intergranular crack in high-strength martensitic steel, Acta Mater. 234 (2022).
[8] J.F. Zhang, D.S. Zhou, X.Y. Pang, B.W. Zhang, Y. Li, B.H. Sun, R.Z. Valiev, D. L. Zhang, Deformation-induced concurrent formation of 9R phase and twins in a nanograined aluminum alloy, Acta Mater. 244 (2023).
[9] B. Gault, A. Chiaramonti, O. Cojocaru-Mirédin, P. Stender, R. Dubosq, C. Freysoldt, S.K. Makineni, T. Li, M. Moody, J.M. Cairney, Atom probe tomography, Nat. Rev. Method. Prim. 1 (1) (2021).
[10] E.A. Marquis, J.M. Hyde, Applications of atom-probe tomography to the characterisation of solute behaviours, Mat Sci Eng R 69 (4–5) (2010) 37–62.
[11] R.K.W. Marceau, L.T. Stephenson, C.R. Hutchinson, S.P. Ringer, Quantitative atom probe analysis of nanostructure containing clusters and precipitates with multiple length scales, Ultramicroscopy 111 (6) (2011) 738–742.
[12] S. Jiang, X. Xu, W. Li, B. Peng, Y. Wu, X. Liu, H. Wang, X. Wang, Z. Lu, Strain hardening mediated by coherent nanoprecipitates in ultrahigh-strength steels, Acta Mater. 213 (2021) 116984.
[13] X.-x. Yu, A. Gulec, K.L. Cwalina, J.R. Scully, L.D. Marks, New insights on the role of chloride during the onset of local corrosion: TEM, APT, surface energy, and morphological instability, Corrosion 75 (6) (2019) 616–627.
[14] B. Gwalani, R.M. Pohan, O.A. Waseem, T. Alam, S.H. Hong, H.J. Ryu, R. Banerjee, Strengthening of Al0. 3CoCrFeMnNi-based ODS high entropy alloys with incremental changes in the concentration of Y2O3, Scripta Mater. 162 (2019) 477–481.
[15] T. Klein, M. Schachermayer, F. Mendez-Martin, T. Schöberl, B. Rashkova, H. Clemens, S. Mayer, Carbon distribution in multi-phase γ-TiAl based alloys and its influence on mechanical properties and phase formation, Acta Mater. 94 (2015) 205–213.
[16] W.T. Sun, J.S. Luo, Y.Y. Chan, J.H. Luan, X.S. Yang, An extraordinary-performance gradient nanostructured Hadfield manganese steel containing multi-phase nanocrystalline-amorphous core-shell surface layer by laser surface processing, J. Mater. Sci. Technol. 134 (2023) 209–222.
[17] K. Hoummada, D. Mangelinck, B. Gault, M. Cabié, Nickel segregation on dislocation loops in implanted silicon, Scripta Mater. 64 (5) (2011) 378–381.
[18] T.F. Yang, S.Q. Xia, W. Guo, R. Hu, J.D. Poplawsky, G. Sha, Y. Fang, Z.F. Yan, C. X. Wang, C.Y. Li, Y. Zhang, S.J. Zinkle, Y.G. Wang, Effects of temperature on the irradiation responses of AlCoCrFeNi high entropy alloy, Scripta Mater. 144 (2018) 31–35.
[19] X. Zhou, Y. Wei, M. Kühbach, H. Zhao, F. Vogel, R.D. Kamachali, G.B. Thompson, D. Raabe, B. Gault, Revealing in-plane grain boundary composition features through machine learning from atom probe tomography data, Acta Mater. 226 (2022) 117633.
[20] A.S. Ebner, S. Jakob, H. Clemens, R. Pippan, V. Maier-Kiener, S. He, W. Ecker, D. Scheiber, V.I. Razumovskiy, Grain boundary segregation in Ni-base alloys: a combined atom probe tomography and first principles study, Acta Mater. 221 (2021) 117354.
[21] O.C. Hellman, J.B. du Rivage, D.N. Seidman, Efficient sampling for three-dimensional atom probe microscopy data, Ultramicroscopy 95 (1–4) (2003) 199–205.
[22] O.C. Hellman, J.A. Vandenbroucke, J. Rüsing, D. Isheim, D.N. Seidman, Analysis of three-dimensional atom-probe data by the proximity histogram, Microsc. Microanal. 6 (5) (2000) 437–444.
[23] L.T. Stephenson, M.P. Moody, P.V. Liddicoat, S.P. Ringer, New techniques for the analysis of fine-scaled clustering phenomena within atom probe tomography (APT) data, Microsc. Microanal. 13 (6) (2007) 448–463.
[24] A. Shariq, T. Al-Kassab, R. Kirchheim, R.B. Schwarz, Exploring the next neighbourhood relationship in amorphous alloys utilizing atom probe tomography, Ultramicroscopy 107 (9) (2007) 773–780.
[25] D. Vaumousse, A. Cerezo, P. Warren, A procedure for quantification of precipitate microstructures from three-dimensional atom probe data, Ultramicroscopy 95 (2003) 215–221.
[26] J. Zelenty, A. Dahl, J. Hyde, G.D. Smith, M.P. Moody, Detecting clusters in atom probe data with Gaussian mixture models, Microsc. Microanal. 23 (2) (2017) 269–278.
[27] I. Ghamarian, E. Marquis, Hierarchical density-based cluster analysis framework for atom probe tomography data, Ultramicroscopy 200 (2019) 28–38.
[28] Y. Li, Y. Wei, Z. Wang, X. Liu, T. Colnaghi, L. Han, Z. Rao, X. Zhou, L. Huber, R. Dsouza, Quantitative three-dimensional imaging of chemical short-range order via machine learning enhanced atom probe tomography, Nat. Commun. 14 (1) (2023) 7410.

[29] S.K. Makineni, A. Kumar, M. Lenz, P. Kontis, T. Meiners, C. Zenk, S. Zaefferer, G. Eggeler, S. Neumeier, E. Spiecker, D. Raabe, B. Gault, On the diffusive phase transformation mechanism assisted by extended dislocations during creep of a single crystal CoNi-based superalloy, Acta Mater. 155 (2018) 362–371.

[30] C. Varvenne, A. Luque, W.A. Curtin, Theory of strengthening in fcc high entropy alloys, Acta Mater. 118 (2016) 164–176.

[31] Y. Yang, C.-C. Chen, M. Scott, C. Ophus, R. Xu, A. Pryor, L. Wu, F. Sun, W. Theis, J. Zhou, Deciphering chemical order/disorder and material properties at the single-atom level, Nature 542 (7639) (2017) 75–79.

[32] R. Zhang, S. Zhao, J. Ding, Y. Chong, T. Jia, C. Ophus, M. Asta, R.O. Ritchie, A. M. Minor, Short-range order and its impact on the CrCoNi medium-entropy alloy, Nature 581 (7808) (2020) 283–287.

[33] H.-H. Wu, L.-S. Dong, S.-Z. Wang, G.-L. Wu, J.-H. Gao, X.-S. Yang, X.-Y. Zhou, X.-P. Mao, Local chemical ordering coordinated thermal stability of nanograined high-entropy alloys, Rare Metals 42 (5) (2023) 1645–1655.

[34] B. Gault, M.P. Moody, J.M. Cairney, S.P. Ringer, Atom Probe Microscopy, Springer Science & Business Media, 2012.

[35] M.K. Miller, R.G. Forbes, M.K. Miller, R.G. Forbes, The Local Electrode Atom Probe, Springer, 2014.

[36] D.N. Seidman, Three-dimensional atom-probe tomography: advances and applications, Annu Rev Mater Res 37 (2007) 127–158.

[37] R.K.W. Marceau, A.V. Ceguerra, A.J. Breen, D. Raabe, S.P. Ringer, Quantitative chemical-structure evaluation using atom probe tomography: short-range order analysis of Fe-Al, Ultramicroscopy 157 (2015) 12–20.

[38] Y. Li, X. Zhou, T. Colnaghi, Y. Wei, A. Marek, H. Li, S. Bauer, M. Rampp, L. T. Stephenson, Convolutional neural network-assisted recognition of nanoscale L12 ordered structures in face-centred cubic alloys, npj Comput. Mater. 7 (1) (2021).

[39] F. Vurpillot, G. Da Costa, A. Menand, D. Blavette, Structural analyses in three-dimensional atom probe: a Fourier transform approach, J Microsc-Oxford 203 (2001) 295–302.

[40] T. Boll, T. Al-Kassab, Y. Yuan, Z.G. Liu, Investigation of the site occupation of atoms in pure and doped TiAl/Ti3Al intermetallic, Ultramicroscopy 107 (9) (2007) 796–801.

[41] M.P. Moody, B. Gault, L.T. Stephenson, D. Haley, S.P. Ringer, Qualification of the tomographic reconstruction in atom probe by advanced spatial distribution map techniques, Ultramicroscopy 109 (7) (2009) 815–824.

[42] A. Mikhalychev, S. Vlasenko, T. Payne, D. Reinhard, A. Ulyanenkov, Bayesian approach to automatic mass-spectrum peak identification in atom probe tomography, Ultramicroscopy 215 (2020) 113014.

[43] F. Meisenkothen, D. Samarov, M. McLean, I. Kalish, E. Steel, Adaptive Peak Fitting for Isotope Analysis via Atom Probe Mass Spectrometry, Microsc. Microanal. 27 (S1) (2021) 176–177.

[44] K.J. Coakley, N.A. Sanford, Learning Atom Probe Tomography time-of-flight peaks for mass-to-charge ratio spectrometry, Ultramicroscopy 237 (2022) 113521.

[45] Y. Wei, R.S. Varanasi, T. Schwarz, L. Gomell, H. Zhao, D.J. Larson, B.H. Sun, G. Liu, H. Chen, D. Raabe, B. Gault, Machine-learning-enhanced time-of-flight mass spectrometry analysis, Patterns 2 (2) (2021).

[46] S. Madireddy, D.-W. Chung, T. Loeffler, S.K. Sankaranarayanan, D.N. Seidman, P. Balaprakash, O. Heinonen, Phase segmentation in atom-probe tomography using deep learning-based edge detection, Sci Rep 9 (1) (2019) 20140.

[47] Q. Zhao, Q. Zhu, Z. Zhang, X. Li, Q. Huang, W. Yang, J. Wang, H. Gao, H. Zhou, Imaging of atomic stress at grain boundaries based on machine learning, J. Mech. Phys. Solids 181 (2023) 105455.

[48] M. Kühbach, A.J. London, J. Wang, D.K. Schreiber, F.M. Martin, I. Ghamarian, H. Bilal, A.V. Ceguerra, Community-driven methods for open and reproducible software tools for analyzing datasets from atom probe microscopy, Microsc. Microanal. 28 (4) (2022) 1038–1053.

[49] B. Gault, M.P. Moody, J.M. Cairney, S.P. Ringer, Atom probe crystallography, Mater. Today 15 (9) (2012) 378–386.

[50] Y. Wei, B. Gault, R.S. Varanasi, D. Raabe, M. Herbig, A.J. Breen, Machine-learning-based atom probe crystallographic analysis, Ultramicroscopy 194 (2018) 15–24.

[51] M. Kühbach, M. Kasemer, B. Gault, A. Breen, Open and strong-scaling tools for atom-probe crystallography: high-throughput methods for indexing crystal structure and orientation, J. Appl. Crystallogr. 54 (2021) 1490–1508.

[52] Y. Li, T. Colnaghi, Y. Gong, H. Zhang, Y. Yu, Y. Wei, B. Gan, M. Song, A. Marek, M. Rampp, Machine learning-enabled tomographic imaging of chemical short-range atomic ordering, arXiv preprint arXiv:2303.13433 (2023).

[53] K. Yan, Y. Xu, J. Niu, Y. Wu, Y. Li, B. Gault, S. Zhao, X. Wang, Y. Li, J. Wang, Unraveling the origin of local chemical ordering in Fe-based solid-solutions, Acta Mater. (2023) 119583.

[54] Z.Y. Rao, Y. Li, H.B. Zhang, T. Colnaghi, A. Marek, M. Rampp, B. Gault, Direct recognition of crystal structures via three-dimensional convolutional neural networks with high accuracy and tolerance to random displacements and missing atoms, Scripta Mater. 234 (2023).

[55] C.R. Qi, H. Su, K. Mo, L.J. Guibas, Pointnet: deep learning on point sets for 3d classification and segmentation, in: IEEE Conf. Comput. Vis. Pattern Recognit, 2017, pp. 652–660.

[56] B. Gault, X.Y. Cui, M.P. Moody, F. De Geuser, C. Sigli, S.P. Ringer, A. Deschamps, Atom probe microscopy investigation of Mg site occupancy within δ′ precipitates in an Al-Mg-Li alloy, Scripta Mater. 66 (11) (2012) 903–906.

[57] M. Garcia-Gonzalez, S. Van Petegem, N. Baluc, S. Hocine, M. Dupraz, F. Lalire, H. Van Swygenhoven, Enhanced precipitate growth at reduced temperatures during chemical ordering in deformed red gold alloys, Scripta Mater. 170 (2019) 129–133.

[58] B. Gault, M.P. Moody, F. De Geuser, G. Tsafnat, A. La Fontaine, L.T. Stephenson, D. Haley, S.P. Ringer, Advances in the calibration of atom probe tomographic reconstruction, J. Appl. Phys. 105 (3) (2009).

[59] B. Gault, F. de Geuser, L.T. Stephenson, M.P. Moody, B.C. Muddle, S.P. Ringer, Estimation of the reconstruction parameters for atom probe tomography, Microsc. Microanal. 14 (4) (2008) 296–305.

[60] F. Chollet, Deep Learning With Python, Simon and Schuster, 2021.

[61] B. Gault, B. Klaes, F.F. Morgado, C. Freysoldt, Y. Li, F. De Geuser, L.T. Stephenson, F. Vurpillot, Reflections on the Spatial Performance of Atom Probe Tomography in the Analysis of Atomic Neighborhoods, Microsc. Microanal. 28 (4) (2022) 1116–1126.

[62] F. De Geuser, B. Gault, Metrology of small particles and solute clusters by atom probe tomography, Acta Mater. 188 (2020) 406–415.

[63] I. Wallach, M. Dzamba, A. Heifets, AtomNet: a deep, convolutional neural network for bioactivity prediction in structure-based drug discovery, Abstr Pap Am Chem S 251 (2016).

[64] R. Feinman, B.M. Lake, Learning Inductive Biases with Simple Neural Networks, ArXiv abs/1802.02745 (2018).

[65] T. Ishida, I. Yamane, T. Sakai, G. Niu, M. Sugiyama, Do we need zero training loss after achieving zero training error?, arXiv preprint arXiv:2002.08709 (2020).

[66] A. Deschamps, C. Sigli, T. Mourey, F. de Geuser, W. Lefebvre, B. Davo, Experimental and modelling assessment of precipitation kinetics in an Al-Li-Mg alloy, Acta Mater. 60 (5) (2012) 1917–1928.

[67] Y. Li, B. Holmedal, H. Li, L. Zhuang, J. Zhang, Q. Du, Precipitation and strengthening modeling for disk-shaped particles in aluminum alloys: size distribution considered, Materialia 4 (2018) 431–443.

[68] Z. Zhang, Y. Li, H. Li, D. Zhang, Z. Zhao, Q. Du, J. Zhang, ICME guided design of heat-treatable Zn-modified Al–Mg alloys, Calphad 74 (2021) 102298.

[69] B.P. Geiser, T.F. Kelly, D.J. Larson, J. Schneir, J.P. Roberts, Spatial distribution maps for atom probe tomography, Microsc. Microanal. 13 (6) (2007) 437–447.

[70] M.N.D. Larcher, C. Cayron, A. Blatter, R. Soulignac, R.E. Logé, length The thermally activated distortion with amplification effect and related variant selection in red gold alloys, Acta Mater. 198 (2020) 242–256.

[71] H. Ghasemi-Tabasi, M.D. Larcher, C. Cayron, J. Jhabvala, S. Van Petegem, N. E. Kalentics, E. Boillat, R. Loge, Understanding variant selection and texture in additively manufactured red-gold alloys, Scripta Mater. 211 (2022).

[72] S. Wei, C.C. Tasan, Deformation faulting in a metastable CoCrNiW complex concentrated alloy: a case of negative intrinsic stacking fault energy? Acta Mater. 200 (2020) 992–1007.

[73] L. Kovarik, R.R. Unocic, J. Li, P. Sarosi, C. Shen, Y. Wang, M.J. Mills, Microtwinning and other shearing mechanisms at intermediate temperatures in Ni-based superalloys, Prog. Mater Sci. 54 (6) (2009) 839–873.

[74] W.C. Yang, P.F. Qu, J.C. Sun, Q.Z. Yue, H.J. Su, J. Zhang, L. Liu, Effect of alloying elements on stacking fault energies of γ and γ' phases in Ni-based superalloy calculated by first principles, Vacuum 181 (2020).

[75] A. Bezold, S. Neumeier, Tailoring deformation mechanisms in polycrystalline CoNi-base superalloys for enhanced high temperature strength, Scripta Mater. 226 (2023).

[76] P. Pandey, M. Heczko, N. Khatavkar, N. Mazumder, A. Sharma, A. Singh, M. J. Mills, K. Chattopadhyay, On the faulting and twinning mediated strengthening and plasticity in a γ' strengthened CoNi-based superalloy at room temperature, Acta Mater. 252 (2023) 118928.

[77] T.M. Smith, N.A. Zarkevich, A.J. Egan, J. Stuckner, T.P. Gabb, J.W. Lawson, M. J. Mills, Utilizing local phase transformation strengthening for nickel-base superalloys, Commun Mater 2 (1) (2021).

[78] L.S. Feng, S.B. Kannan, A. Egan, T. Smith, M.J. Mills, M. Ghazisaeidi, Y.Z. Wang, Localized phase transformation at stacking faults and mechanism-based alloy design, Acta Mater. 240 (2022).

[79] S. Antonov, B. Li, B. Gault, Q. Tan, The effect of solute segregation to deformation twin boundaries on the electrical resistivity of a single-phase superalloy, Scripta Mater. 186 (2020) 208–212.

[80] J.Y. He, C.H. Zenk, X.Y. Zhou, S. Neumeier, D. Raabe, B. Gault, S.K. Makineni, On the atomic solute diffusional mechanisms during compressive creep deformation of a Co-Al-W-Ta single crystal superalloy, Acta Mater. 184 (2020) 86–99.

[81] S.K. Makineni, M. Lenz, P. Kontis, Z. Li, A. Kumar, P.J. Felfer, S. Neumeier, M. Herbig, E. Spiecker, D. Raabe, B. Gault, Correlative Microscopy-Novel Methods and Their Applications to Explore 3D Chemistry and Structure of Nanoscale Lattice Defects: a Case Study in Superalloys, JOM 70 (9) (2018) 1736–1743.

[82] C. Ledig, L. Theis, F. Huszár, J. Caballero, A. Cunningham, A. Acosta, A. Aitken, A. Tejani, J. Totz, Z. Wang, Photo-realistic single image super-resolution using a generative adversarial network, in: IEEE Conf. Comput. Vis. Pattern Recognit, 2017, pp. 4681–4690.

[83] R. Rombach, A. Blattmann, D. Lorenz, P. Esser, B. Ommer, High-resolution image synthesis with latent diffusion models, in: IEEE/CVF Conf. Comput. Vis. Pattern Recognit, 2022, pp. 10684–10695.